ACS OMEGA

Article

Cite This: ACS Omega 2018, 3, 3384−3395

Purely Inorganic Highly Efficient Ice Nucleating Particle

Mainak Ganguly,[†] Simon Dib,[‡] and Parisa A. Ariya*[,†,‡]

[†]Department of Atmospheric and Oceanic Sciences, McGill University, Montreal, Quebec H3A 0B9, Canada

[‡]Department of Chemistry, McGill University, Montreal, Quebec H3A 0B8, Canada

Supporting Information

ABSTRACT: To evaluate the role of atmospheric heterogeneous reactions on the ice nucleation ability of airborne dust particles, we investigated the systematic study of ice nucleation microphysics with a suite of atmospherically relevant metals (10), halides (4), and oxyhalides (2). Within a minute, a kaolin−iron oxide composite (KaFe) showed efficient reactions with aqueous mercury salts. Among the different mercury salts tested, only $HgCl_2$ reacting with KaFe generated HgKaFe, a highly efficient ice nucleating particle (HEIN). When added to water, HgKaFe caused water to freeze at much warmer temperatures, within a narrow range of −6.6 to −4.7 °C. Using a suite of optical spectroscopy, mass spectrometry, and microscopy techniques, we performed various experiments to decipher the physical and chemical properties of surface and bulk. KaFe was identified as a mixture of different iron oxides, namely, goethite, hematite, magnetite, and ε-Fe_2O_3, with kaolin. In HgKaFe, $HgCl_2$ was reduced to Hg_2Cl_2 and iron was predominantly in maghemite form. Reduction of Fe^{2+} by $NaBH_4$, followed by aerial oxidation, helped KaFe to be an exact precursor for the synthesis of HEIN HgKaFe. Kaolin served as a template for synthesizing iron oxide, opposing unwanted aggregation. No other metal or metal halide was found to have more efficient nucleating particles than $HgCl_2$ with KaFe composite. The chelation of Hg(II) hindered the formation of HEIN. This study is useful for investigating the role of morphology and how inorganic chemical reactions on the surface of dust change morphology and thus ice nucleation activity. The understanding of the fundamentals of what makes a particle to be a good ice nucleating particle is valuable to further understand and predict the amount and types of atmospheric ice nucleating particles.

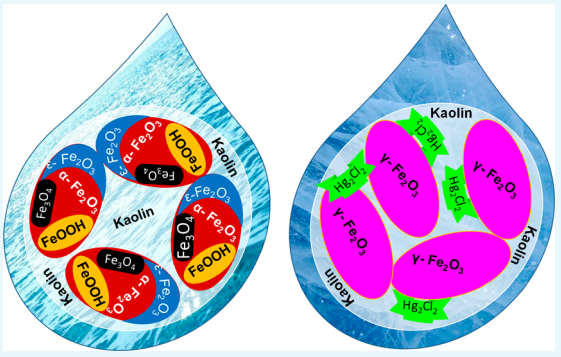

1. INTRODUCTION

Iron-rich kaolin is found in many places on Earth.[1] Kaolin seldom possesses aluminum oxides or hydroxides. Weathering and degradation of feldspars and other aluminosilicates result in the formation of kaolin, transported by the wind in the atmosphere. This process includes the elimination of various cations and the product with contaminants.[1] Fe is a common contaminant of kaolin and often leaches from kaolin to precipitate as oxide or oxyhydroxide.[2] The laminated limestones of the Late Triassic Mohila Formation (Makhtesh Ramon, Israel) are interbedded with dolomite, gypsum, and some illite, kaolinite (mostly Fe-rich), and mixed-layer clay.[3,4] Various mining and fossil fuel power generation activities have also shown the concurrent emission of dusts containing iron and various clay minerals like kaolin, as well as trace metals, such as mercury.[5]

Nanoparticles are ubiquitous in the atmosphere and are known to be of the utmost importance by both health and climate organizations. Adams et al.[6] vividly explained the role nanoparticles play in climate change. Similarly, Gwinn and Vallyathan demonstrated the pros and cons of nanoparticles on health.[7] As a matter of fact, nanoparticle-induced ice nucleation is an important field of study, in relation to climate and health.[8]

The ice nucleation phenomenon is something that we experience almost regularly in a variety of scenarios, including climate change and intracellular freezing.[9−12] Pure supercooled water can be cooled to ca. −40 °C without freezing.[9] However, the ice nucleation phenomena in nature occurs very often due to the nucleating substances, ranging from nanoparticles and biological compounds to crystalline surfaces. The remarkable diversity in nucleating compounds makes the mechanism of ice nucleation by efficient ice nucleating particles very complicated.[13] Since the last few decades, a great deal of experimental and theoretical research has been undertaken to reveal the unequivocal driving force for efficient ice nucleation. However, the understanding of heterogeneous ice nucleation is quite complex, and its physicochemical intricacy has yet to be deciphered.

During the last five decades, several organic and inorganic materials have been suggested to contribute to ice nucleation.[14−18] To date, the best ice nucleating particles have been selected bacteria, including Gram-negative *Pseudomonas syringae*, which freeze at about −2 °C.[14] Yet, due to the propensity of dust particles globally, the overall impact of dust particles on ice nucleation has been considered to be very important.

Mineral dusts are ubiquitous in the atmosphere and contain various metals and minerals, including a suite of metals, metal

Received: November 21, 2017
Accepted: January 31, 2018
Published: March 20, 2018

DOI: 10.1021/acsomega.7b01830
ACS Omega 2018, 3, 3384−3395

oxides, and clay minerals, such as kaolin. Many studies related to the efficiency of mineral dust and acid-coated mineral dust have been conducted for heterogeneous ice nucleation at cirrus temperatures. Because of the abundance in observed aerosols around the world, various types of iron oxides have been employed as a surrogate for environmental mineral dust particles.[15] Furthermore, some studies have provided identification of efficiency of ice nucleation by generating active sites of clay particles, like feldspar, kaolin, and montmorillonite, with or without metal particles.[16−18]

It has been increasingly clear that atmospheric aerosols are mostly not homogenous in composition or phase. Many studies indicate that several ice nucleating particles in the atmosphere and at atmospheric interfaces (air/snow/ice/water/soil) can be heterogeneous in composition with multiphase configurations.[19] Yet, the impact of co-pollutants and the physical and chemical processes leading to the change of nucleation processes are still unknown.

Along with the possible uptake of aerosols, mercury species may partake in nucleation, leading to a phase alteration, from a less condensed to a more condensed phase.[20] Iron particles in the nanoregime have been proven to be excellent platforms to uptake many kinds of metal ions.[21,22] Liu et al.[23] demonstrated density functional theory (DFT) as well as conducted experimental studies on the mechanism of elemental mercury capture, in the presence of HCl on α-Fe_2O_3(001). Further experimental and theoretical works are yet to be done to understand the effect of a toxic metal, like mercury, on clay particles containing other metals.

In this study, we investigated the ice nucleation ability of the combination of a suite of metal and metal oxides as well as inorganic halogenated compounds of relevance to the atmosphere and to atmospheric surfaces. Among several freezing modes, we followed immersion freezing mode using drop-freezing experiments to understand the ice nucleation efficiency.[24,25] We provide the evidence for a kaolin−iron oxide composite (KaFe) that absorbs $HgCl_2$ in water. Through a complementary suite of spectroscopic and microscopic techniques, we provide physical and chemical insights of our observations and a potential reaction mechanism.

2. RESULTS AND DISCUSSION

2.1. Characterization of KaFe and HgKaFe. We performed complementary synthesis, characterization, and microphysics studies. The following section explores all systematic steps that led to the identification of effective ice nucleating particles. This can expand the range of known ice nucleating materials, particularly with more diverse emissions of emerging nanoparticle contaminants in the atmosphere coming to light. The mean freezing temperature (MFT) is a measure of the ice nucleation ability of nucleating particles. Brooks et al. compared ice nucleation activity of soot and polycyclic aromatic hydrocarbons using the mean freezing temperature (MFT).[26] For the purpose of clarity in describing the relative ice nucleation temperature patterns of various ice nucleating particles studied in this work, particles with a mean freezing temperature <7 °C were classified as highly efficient ice nucleating particles (HEINs), those with a mean freezing temperature in between −14 and −7 °C were termed as average ice nucleating particles, and the particles with a mean freezing temperature in between −21 and −14 °C were termed as poor ice nucleating particles.

KaFe was a gray solid, synthesized from off-white kaolin and greenish yellow $FeCl_2{\cdot}4H_2O$, after treatment with sodium borohydride. Our experiment showed that the freezing range of KaFe was −20.2 to −8.8 °C (poor ice nucleating particles with MFT of −16.7 °C) when HgKaFe (KaFe@$HgCl_2$) was a HEIN. No other metal chloride, except $HgCl_2$, demonstrated high ice nucleation ability with KaFe, as illustrated in Figure 1. To

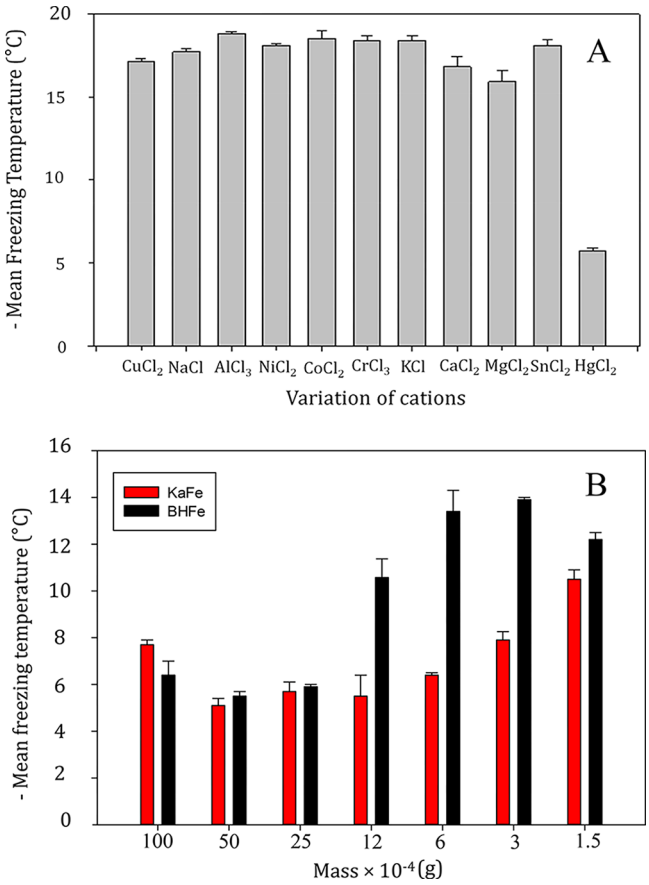

Figure 1. (A) Bar diagram representing the mean freezing temperature of 3.69×10^{-3} M different metal chloride solution with 0.0025 g of KaFe in 10 mL of Milli-Q water. (B) Bar diagram representing the mean freezing temperature of 3.69×10^{-3} M $HgCl_2$ with different amounts of BHFe and KaFe in 10 mL of Milli-Q water.

comprehend its ice nucleation efficiency, knowledge on its physicochemical state is pivotal. Therefore, we characterized KaFe and HgKaFe via microscopic and spectroscopic techniques to understand the drastic differences of ice nucleation properties.

To understand the surface morphology, scanning electron microscopy (SEM) analysis was performed. Pure kaolin was found to be as a stacked nanodish under a scanning electron microscope, whereas in KaFe, particles were attached to the dish as spheres and long wires (made of a small unit sphere of ca. 60−80 nm). However, in BHFe (HEIN), obtained by $NaBH_4$ treatment with $FeCl_2{\cdot}4H_2O$, particles were arranged mostly as aggregated nanowire. Nanospheres and nanowires in KaFe were converted to nanodots on the surface of kaolin in HgKaFe. Energy-dispersive X-ray spectrometry analysis indicated that HgKaFe had more oxygen than KaFe (Figures 2 and S1, Supporting Information). X-ray diffraction (XRD) analyses, discussed below, indicated that KaFe possesses iron oxide. Thereby, iron was further oxidized in HgKaFe. Also, $HgCl_2$ was reduced to Hg_2Cl_2 in the presence of KaFe. Transmission electron microscopy (TEM) analysis supported BHFe to be more aggregated in comparison to KaFe. From high-resolution

DOI: 10.1021/acsomega.7b01830
ACS Omega 2018, 3, 3384−3395

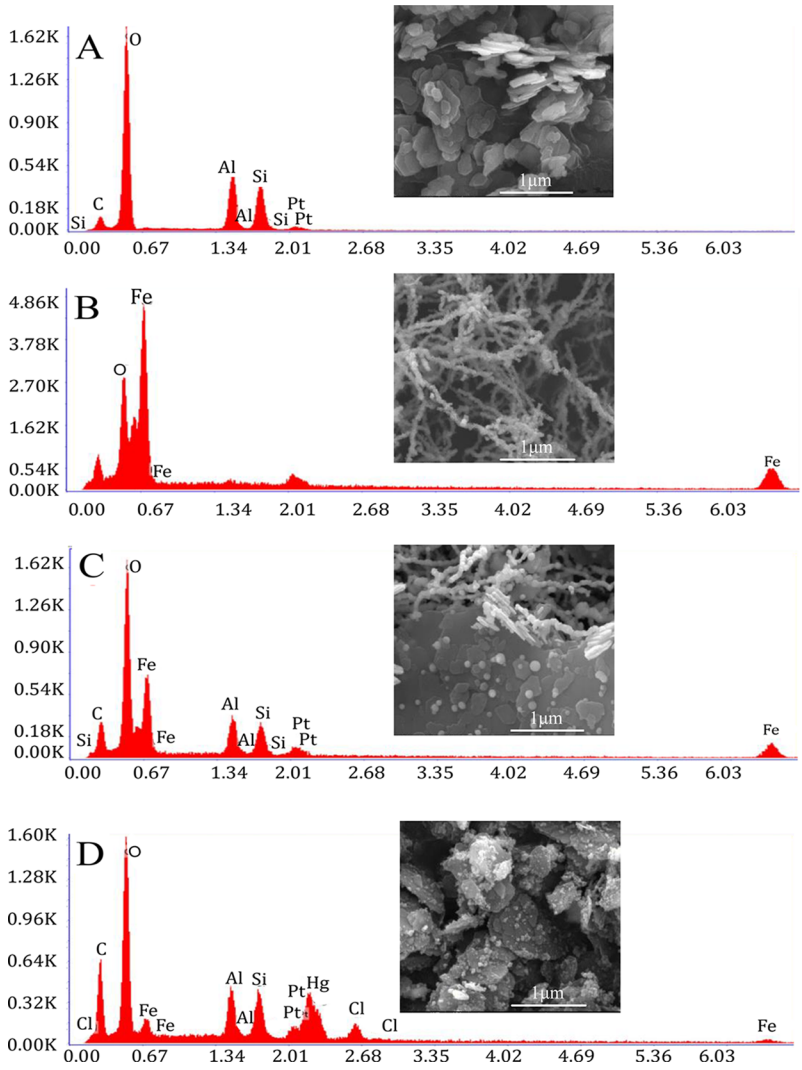

Figure 2. Selected SEM images and EDAX images of (A) kaolin, (B) BHFe, (C) KaFe, and (D) HgKaFe.

transmission electron microscopy (HRTEM) analysis, it became evident that KaFe contained magnetite (Fe_3O_4) as well as goethite (FeOOH). A lattice fringe of 0.29 nm corresponds to the (220) lattice plane of Fe_3O_4, whereas a lattice fringe of 0.47 nm corresponds to FeOOH.[27−29] Furthermore, a lattice fringe of 0.47 nm may likely be due to the (002) plane of ε-Fe_2O_3 (reported lattice fringe of 0.48 nm).[30] On the other hand, a lattice fringe of 0.47 nm was found at different regions of HgKaFe for the (111) plane of maghemite (γ-Fe_2O_3), as depicted in Figure 3.[27]

XRD analysis indicated that KaFe contained ε-Fe_2O_3 (20.3%), hematite (16.1%), goethite (10.2%), and magnetite (4.6%). However, HgKaFe contained maghemite-C, syn (11.9%). Therefore, HgKaFe predominantly possessed one type of iron oxide, i.e., maghemite. Figures 4 and S2−S4, in the Supporting Information, represent the XRD spectra and structural fitting pattern details of KaFe and HgKaFe. In HgKaFe, $HgCl_2$ was reduced to Hg_2Cl_2. As such, during the in situ process, a maghemite−Hg_2Cl_2 composite was produced with HEIN characteristics.

From X-ray photoelectron spectroscopy (XPS) analysis, we found that both KaFe (711.48 eV) and HgKaFe (711.38 eV) had similar oxidation states to Fe(III) $2p_{3/2}$ oxide. Satellite peaks found in both KaFe and HgKaFe indicated that neither compound contained only magnetite.[31] The HgKaFe peak for the binding energy of Hg was 101.08−101.48 eV. This peak might be due to the presence of some unreacted $HgCl_2$, along with Hg_2Cl_2 (calomel).[32] A shift in binding energy of Hg(I) $4f_{7/2}$ toward a higher-energy region was the result of the anchoring of Hg_2Cl_2 to electron-deficient iron oxide maghemite. The main components of kaolin are Al and Si. A decrease in the binding energies of Al 2p and Si 2p in HgKaFe (75.20 eV for Al and 103.06 eV for Si) in comparison to KaFe (75.37 eV for Al and 103.93 eV for Si) indicated that Al and Si were electron-rich by further oxidizing magnetite (Fe_3O_4) to maghemite in HgKaFe. More metal−oxide interactions (~530.3 eV) in HgKaFe than in KaFe implied that a higher concentration of iron(III) oxide was formed mainly in HgKaFe compared to KaFe.[33] It is to be mentioned that Cl^- 2p in $HgCl_2$ did not alter its electronic state in HgKaFe (binding energy, 199.53 eV)[34] (Figures 5 and S5, Supporting Information).

It is important to note that no detectable Hg(0) was emitted from HgKaFe, as determined by mass spectral analysis (shown in Figure 6) under our experimental conditions. Instead of using $NaBH_4$, the use of NH_4OH during the preparation of KaFe resulted in HgKaFe, which is a poor ice nucleating particle (MFT, −16.3 °C). As such, the reduction of iron chloride with $NaBH_4$, followed by aerial oxidation of KaFe, produces HgKaFe

DOI: 10.1021/acsomega.7b01830
ACS Omega 2018, 3, 3384−3395

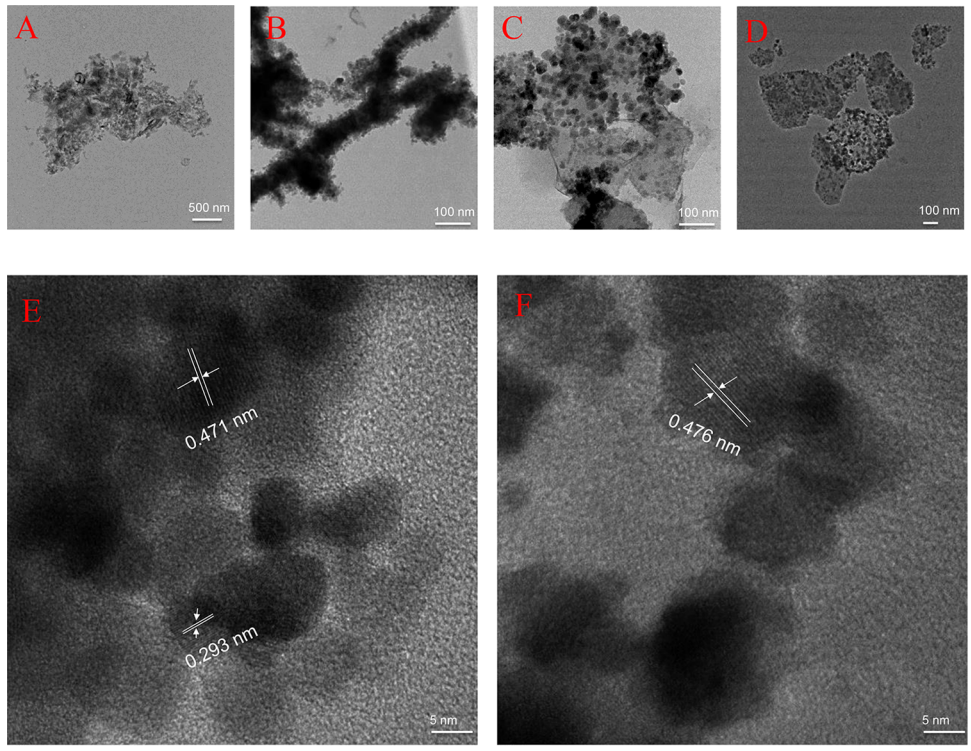

Figure 3. TEM images of (A) kaolin, (B) BHFe, (C) KaFe, and (D) HgKaFe. HRTEM images of (E) KaFe and (F) HgKaFe.

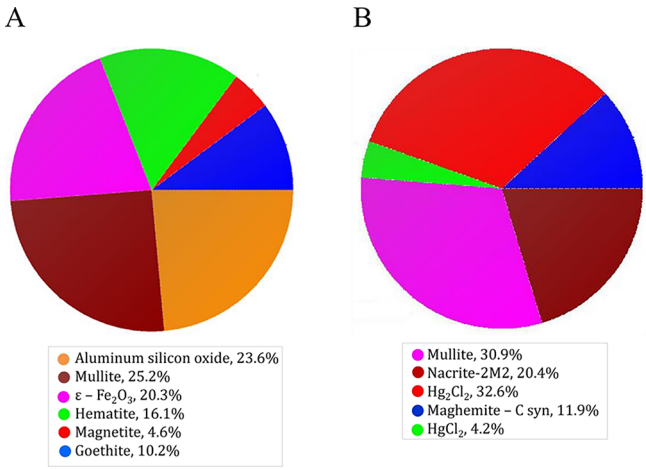

Figure 4. Pie diagram representing the composition of (A) KaFe and (B) HgKaFe, obtained from XRD analysis.

(HEIN) with aqueous $HgCl_2$, as illustrated in Figure S6 in the Supporting Information.

Thin films of kaolin, KaFe, and HgKaFe were made from their aqueous suspensions via spin coating. Then, 10 μL of Milli-Q water was dropped onto each of the films. Subsequently, using a goniometer, we measured the contact angles of the drops. Kaolin and HgKaFe were hydrophilic compounds with measured contact angles of 33 and 32°, respectively. On the contrary, KaFe was very much hydrophilic and its contact angle was 12°, as shown in Figure 6. However, HgKaFe was shown to be the HEIN. A low contact angle generally refers to a higher affinity toward water. Lupi and Molinero[35] discovered that the increment of hydrophilicity can exhibit adverse effects, due to the incorporation of OH groups, reducing water–surface interaction strength. The experiment performed by Whale et al.[36] also supports the aforementioned proposition. Notwithstanding these data, contact angle measurement using thin films should not be the sole conclusive measure to evaluate ice nucleating potentials of particles.

2.2. HEIN HgKaFe. KaFe in water was classified as a poor ice nucleating material, as mentioned above. Similarly, kaolin showed ice nucleation ability within the range of −20 to −12 °C (MFT, −16.2 °C). We subsequently sonicated 0.0025 g of KaFe inside an aqueous solution of 10 mL of 3.69×10^{-3} M $HgCl_2$ for 10 min. Further ice nucleation experiments were carried out, and it was discovered that water froze at much warmer temperatures (−6.6 to −4.7 °C; MFT, −5.6 °C). We note that pure $HgCl_2$ (3.69×10^{-3} M) was also found to be a poor ice nucleating material. An aqueous solution of 3.69×10^{-3} M $HgCl_2$ froze within a range of −17 to −6 °C (MFT, −15.3 °C). HgKaFe, as HEIN, was obtained when 0.0025 g of KaFe was sonicated with 10 mL of a 3.69×10^{-3} M aqueous $HgCl_2$ solution for 10 min. At this point, water froze very quickly within a narrow temperature range of −6.6 to −4.7 °C. $NaBH_4$-treated kaolin (BHKa) was a poor ice nucleating material in water (−21 to −11 °C; MFT, −18.7 °C) or an average ice nucleating material with aqueous $HgCl_2$ (−20 to −8 °C; MFT, −13.5 °C). Interestingly, it was discovered that $NaBH_4$-treated $FeCl_2{\cdot}4H_2O$ (BHFe), without kaolin, was a poor ice nucleating material (−22 to −12 °C; MFT, −17.4 °C). On the contrary, BHFe was a HEIN in aqueous $HgCl_2$ solution (−7.5 to −4.8 °C; MFT, −5.8 °C). Thus, the Fe–Hg composite was indeed a HEIN, whether kaolin was present in the system or not, as depicted in Figure 7A.

Kaolin in KaFe was used as a scaffold for the synthesis of Fe(0) particles, formed initially after the addition of $NaBH_4$. Then, rapid aerial oxidation took place, forming kaolin-passivated iron oxide. It was previously reported that modified zero-valent iron nanoparticles enhance the rapidity and efficacy of remediation.[37,38] During the reduction of an aqueous iron salt, support materials were introduced to prevent the usual aggregation of

DOI: 10.1021/acsomega.7b01830
ACS Omega 2018, 3, 3384−3395

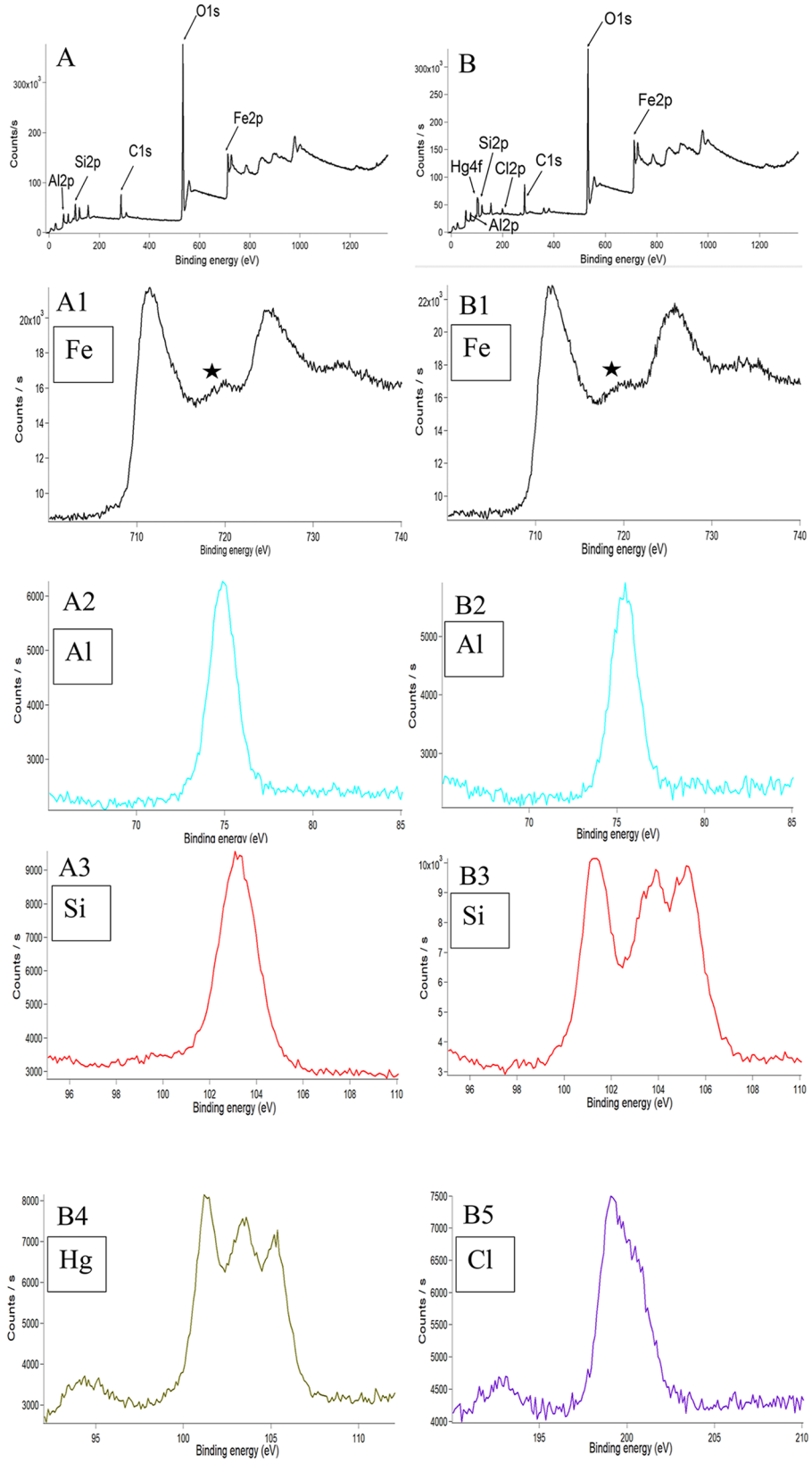

Figure 5. (A, B) Wide-range XPS images of KaFe and HgKaFe. (A1−A3) XPS images of elements Fe, Al, and Si, respectively, in KaFe. (B1−B5) XPS images of elements Fe, Al, Si, Hg, and Cl, respectively, in HgKaFe. The symbol ★ in A1 and B1 represents a satellite peak.

iron nanoparticles, as have been previously reported by Ponder et al.[21] and Zhang et al.[37] Therefore, the dispersion of kaolin-embedded iron oxide nanoparticles (KaFe) exhibited a higher specific surface area. Consequently, a higher reactivity of iron toward the aqueous $HgCl_2$ was observed, and 0.0025 g of solid KaFe (containing less iron than 0.0025 g of solid BHFe) showed improved ice nucleation ability with aqueous $HgCl_2$, compared

DOI: 10.1021/acsomega.7b01830
ACS Omega 2018, 3, 3384−3395

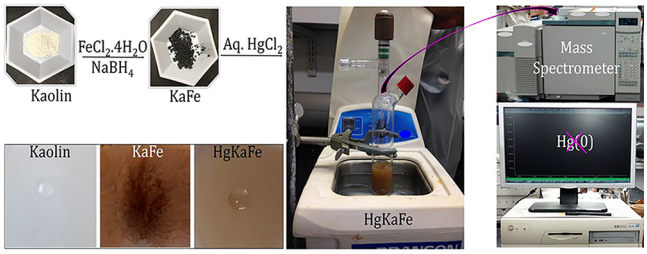

Figure 6. Schematic representation of no Hg(0) vapor evolution from HgKaFe and digital images of 10 μL water droplet on thin films (of kaolin, KaFe, and HgKaFe).

to 0.0025 g of BHFe with aqueous $HgCl_2$ of a similar concentration.

2.3. Impact of the Change of Concentration and Mixing Ratios of Composites on Ice Nucleation. In this study, both KaFe and BHFe were HEIN, with $HgCl_2$. Ice nucleation efficiency was investigated at a wide range of concentrations of KaFe and BHFe with $HgCl_2$. It was discovered that the efficiency of BHFe with $HgCl_2$ as an ice nucleating particle decreased rapidly with decreasing concentration, unlike KaFe. KaFe was a much more efficient nucleating particle (−6.4 to −4.2 °C; MFT, −5.4 °C when 0.0012 g of KaFe was employed) with $HgCl_2$ than BHFe (−11.9 to −7.4 °C; MFT, −10.5 °C when 0.0012 g of BHFe was employed), when the amount was <0.0025 g. This experiment provided evidence for the importance of kaolin as a template and the importance of making KaFe more efficient by protecting the rapid aggregation of iron particles.[39,40] Thereby, under our experimental conditions, kaolin enhanced the surface-to-volume ratio (and active sites at the surface) of iron particles (Figures 1B and S7, Supporting Information).

During the synthesis of KaFe, we varied the concentration ratio of kaolin to $FeCl_2{\cdot}4H_2O$, keeping the amount of kaolin and $NaBH_4$ unchanged. KaFe, prepared from higher [$FeCl_2{\cdot}4H_2O$], was found to be a more efficient ice nucleating particle with $HgCl_2$ [KaFe from $FeCl_2{\cdot}4H_2O$/kaolin = 0.125 with a freezing range of −19.7 to −8.1 °C (MFT, −15.3 °C) with $HgCl_2$, whereas KaFe from $FeCl_2{\cdot}4H_2O$/kaolin = 4.000 with a freezing range of −6.5 to −4.9 °C (MFT, −4.4 °C) with $HgCl_2$]. This indicated that the iron particle was the key player for ice nucleation and kaolin was its template, as depicted in Figure 7B. Besides, change of surface area, morphology, or size of the particles might be altered in KaFe (of altered iron-to-kaolin ratio), resulting in altered ice nucleation ability.

2.4. Importance of $HgCl_2$. Under our experimental conditions, no other studied metal chloride except mercury(II) chloride, namely, copper(II) chloride, sodium(I) chloride, aluminum(III) chloride, nickel(II) chloride, cobalt(II) chloride, chromium(II) chloride, potassium(I) chloride, calcium(II) chloride, magnesium(II) chloride, or tin(II) chloride, could produce HEIN with KaFe. In other words, the Fe−Hg composite was very selective to produce efficient ice nucleating particles, as shown in Figures 1 and S8, in the Supporting Information.

When we increased [$HgCl_2$] gradually with a fixed amount of KaFe (0.0025 g), it was observed that KaFe increased its efficiency as an ice nucleating particle. When 0.0025 g of $HgCl_2$ is used in 10 mL of an aqueous KaFe suspension, the freezing range is −14.9 to −8 °C (MFT, −14 °C). On the other hand, when 0.05 g of $HgCl_2$ was employed in 10 mL of an aqueous KaFe suspension, the freezing range was −5 to −3.5 °C (MFT, −4.2 °C). This indicated that Fe−$HgCl_2$ composites were responsible for HEIN. In other words, iron oxide and $HgCl_2$ were both pivotal to produce HEIN (Figure 7C).

The importance of the chloride ion to form HEIN with KaFe was also evaluated. The experiments above were repeated with other Hg salts, like $Hg(NO_3)_2$, $HgBr_2$, HgI_2, $Hg_2(NO_3)_2$, and HgBr. However, they exhibited relatively poor ice nucleation ability with KaFe, as shown in Figure 7D. It is to be noted that insoluble HgI_2 itself was an average ice nucleating particle (−13.5 to −5.1 °C; MFT, −10.6 °C), due to the remarkable size difference between Hg^{2+} and I^-, as shown in Figure S9 in the Supporting Information. HgI_2 with KaFe was also found to be significantly efficient, but not more efficient than $HgCl_2$. The freezing range of KaFe−HgI_2 (−9.3 to −4.7 °C; MFT, −7.4 °C) was much wider than that of KaFe−$HgCl_2$. However, the improvement of the ice nucleation ability of HgI_2, after the association with KaFe, was not as impressive as with $HgCl_2$. The small improvement in ice nucleation ability of HgI_2 is attributed to the size difference between the cation and anion in the compound, which is related to the ease of ionization. Thus, both Hg and Cl were needed to generate HEIN with KaFe.

After the addition of $Hg(NO_3)_2$ to the aqueous suspension of KaFe, the mixture was sonicated. Subsequently, different sodium salts (NaF, NaCl, NaBr, NaI, $NaClO_3$, and $NaIO_3$) were added individually and sonicated further for 10 min. We found that only NaCl created HEIN, supporting the idea of the pivotal role that Cl^- has in the formation of HEIN. Interestingly, $NaClO_3$ did not produce a HEIN, indicating that the electronic environment of Cl^- was crucial, as shown in Figure 7E. Therefore, free Cl^- might also be a key player, along with Fe and Hg, in the formation of HEIN.

We note that under our experimental conditions, [$Hg(NO_3)_2$ + NaI] with KaFe was found to be an average ice nucleating material (−10.7 to −6.1 °C; MFT, −8.3 °C). After further experiments, we observed that [$Hg(NO_3)_2$ + NaI] without KaFe produced a similar nucleation range of −12.5 to −5.5 °C (MFT, −8.9 °C) (Figure S10, Supporting Information). However, pure HgI_2, due to its hydrophobicity, showed freezing points from −13.5 to −5.1 °C (MFT, −10.5 °C). The size discrepancy between Na^+ and I^- is much higher than that between Hg^{2+} and I^-, facilitating ease of ionization and surface buckling for NaI.

2.5. Effect of Washing of the Precipitate of HgKaFe. HgKaFe (HEIN) was formed when 0.01 g of $HgCl_2$ was added to 10 mL of Milli-Q water, which contained 0.0025 g of KaFe. The precipitate was then centrifuged and later washed several times with Milli-Q water. Ice nucleation experiments were then performed in the presence of 10 mL of Milli-Q water, containing 0.01 g of $HgCl_2$. The efficiency of HgKaFe as an ice nucleating particle was reduced remarkably after the first cycle. We observed freezing points within the range of −6.6 to −4.7 °C (MFT, −5.7 °C) for the first cycle, −14.6 to −8.7 °C (MFT, −12.4 °C) for the second cycle, −16.9 to −7.7 °C (MFT, −12.5 °C) for the third cycle, and −20.5 to −13.3 °C (MFT, −13.8 °C) for the fourth cycle. As such, we could confirm that there was a permanent change in KaFe, after the treatment of $HgCl_2$. Our results indicated that there was an inactivation of the active sites of KaFe. Even after several washes, the original KaFe, which produced HEIN with $HgCl_2$, could not be obtained, as illustrated in Figure 7F.

We examined the ice nucleation efficiency of the precipitate obtained in the HgKaFe solution. The precipitate was washed several times with Milli-Q water and ice nucleation experiments were performed in Milli-Q water. We found that the precipitate (WHgKaFe) was frozen within the range of −23.5 to −13.3 °C

DOI: 10.1021/acsomega.7b01830
ACS Omega 2018, 3, 3384−3395

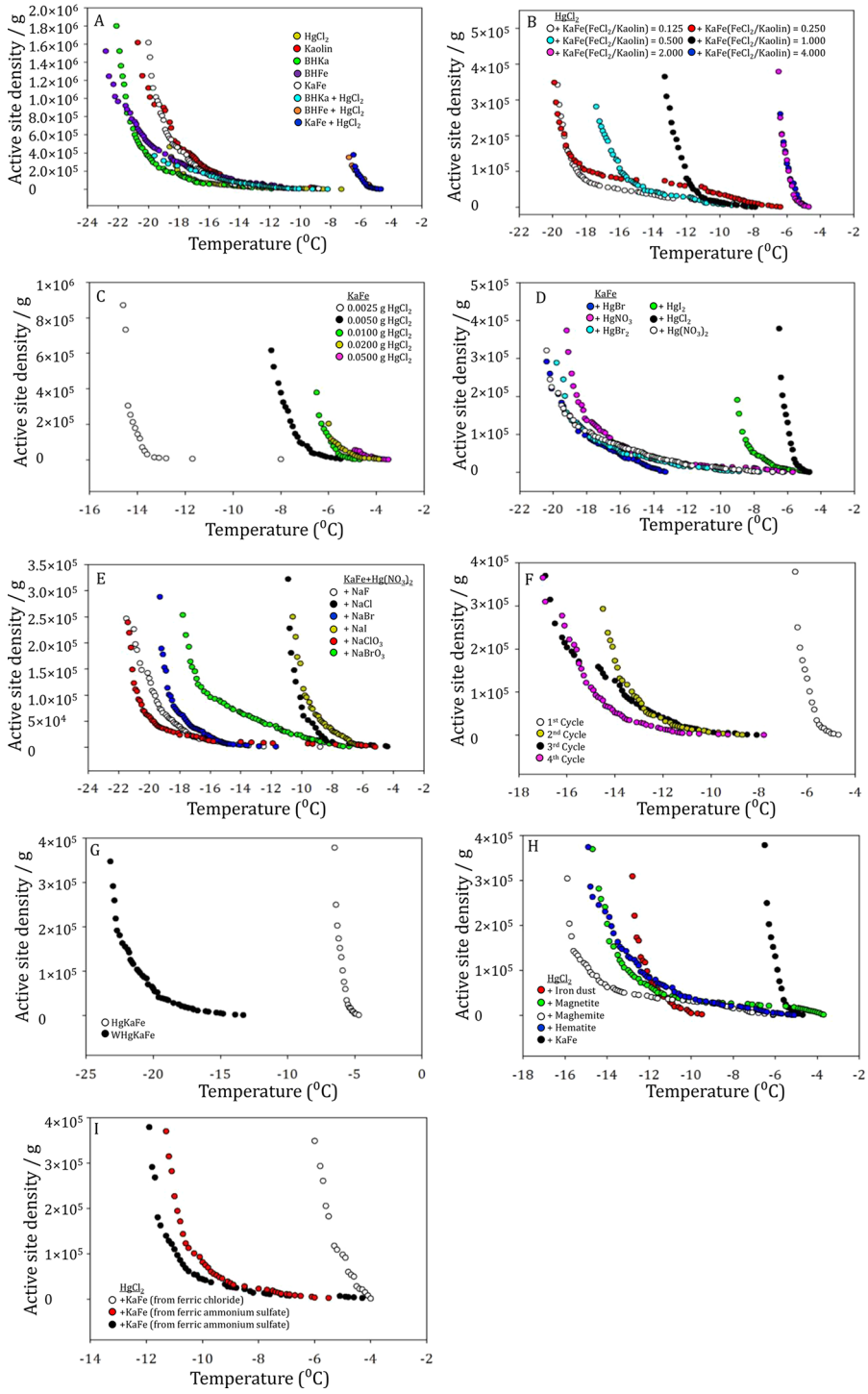

Figure 7. Comparison of active-site density per gram against temperature (in 10 mL of Milli-Q water) of (A) 3.69×10^{-3} M pure $HgCl_2$, 0.0025 g of kaolin, 0.0025 g of BHKa, 0.0025 g of BHFe, 0.0025 g of KaFe, 0.0025 g of BHKa with 3.69×10^{-3} M $HgCl_2$, 0.0025 g of BHFe with 3.69×10^{-3} M $HgCl_2$, 0.0025 g of KaFe with 3.69×10^{-3} M $HgCl_2$; (B) 3.69×10^{-3} M $HgCl_2$ with 0.0025 g of KaFe [prepared with a different ratio of kaolin to $FeCl_2 \cdot 4H_2O$]; (C) $HgCl_2$ of different concentrations (including 3.69×10^{-3} M, i.e., 0.01 g) with 0.0025 g of KaFe; (D) 3.69×10^{-3} M different Hg salts with 0.0025 g of KaFe; (E) 3.69×10^{-3} M $Hg(NO_3)_2$ with 0.0025 g of KaFe in the presence of different sodium salts of 1.7×10^{-2} M; (F) HgKaFe at different cycles; (G) HgKaFe (first cycle) and WHgKaFe; (H) iron dust and different iron oxide (0.0025 g) with $HgCl_2$ (3.69×10^{-3} M); and (I) HgKaFe (KaFe prepared from different iron precursors).

(MFT, −19.5 °C). This indicated that Hg was not strongly adsorbed in the precipitate, as illustrated in Figure 7G. From infrared spectra, we confirmed the existence of KaFe and WHgKaFe using their fingerprinting spectral signatures, as depicted in Figure S11 in the Supporting Information. There was no evidence for the presence of $HgCl_2$ in WHgKaFe.[41]

2.6. Effect of Different Iron Compounds with $HgCl_2$ on Ice Nucleation. To examine potential atmospheric reactions of dust and mercury chlorides, commercially available iron dust

DOI: 10.1021/acsomega.7b01830
ACS Omega 2018, 3, 3384−3395

particles were used, as well as magnetite (Fe_3O_4), maghemite (γ-Fe_2O_3), and hematite (α-Fe_2O_3), to evaluate their ice nucleation efficiency in the presence of $HgCl_2$. We observed the freezing ranges of −12.9 to −6.1 °C (MFT, −11 °C), −14.9 to −3.9 °C (MFT, −10.3 °C), −16 to −5.2 °C (MFT, −12.2 °C), and −15.2 to −5.1 °C (MFT, −10.5 °C) for iron dust particles, magnetite, maghemite, and hematite, respectively. However, the reduction of $FeCl_2{\cdot}4H_2O$ with $NaBH_4$ (in KaFe), followed by aerial oxidation, generated active sites for $HgCl_2$ to sit on, producing HEIN, as illustrated in Figure 7H. From the XRD spectra, it was evident that in KaFe, Fe is in both +2 and +3 oxidation states. However, in HgKaFe, Fe was always observed to be at the +3 oxidation state. Fe in KaFe was further oxidized (OKaFe) and thus completely oxidized to its +3 oxidation state. When using a strong oxidizing agent, hydrogen peroxide (H_2O_2), OKaFe showed a decrease in its ice nucleation ability (−20.1 to −9.2 °C; MFT, −16.5 °C), in the presence of $HgCl_2$ (Figure S12, Supporting Information).

During the synthesis of KaFe, we altered the iron precursors, to explore their impacts on ice nucleation processes. Instead of $FeCl_2{\cdot}4H_2O$, we employed $FeCl_3{\cdot}6H_2O$, ferrous ammonium sulfate, and ferric ammonium sulfate. Our nucleation experiments indicated that $FeCl_3.6H_2O$ also produced KaFe, which was capable of originating HEIN with $HgCl_2$ (−6 to −4 °C; MFT, −4.8 °C). Ferrous ammonium sulfate and ferric ammonium sulfate also produced KaFe, KaFe from ferrous ammonium sulfate with $HgCl_2$, and KaFe from ferric ammonium sulfate with $HgCl_2$, nucleated within the ranges of −12.4 to −4.3 °C (MFT, −9.7 °C) and −11.7 to −5.5 °C (MFT, −9.2 °C), respectively, as shown in Figure 7I. The decreased nucleation efficiency of KaFe from ferric/ferrous ammonium sulfate with $HgCl_2$ is attributed to ammonium sulfate-induced aggregation of iron (rendering lower surface area).

2.7. Absorption of $HgCl_2$ in KaFe. To further provide physical insights into the absorption of $HgCl_2$ in KaFe, several UV−vis spectroscopic experiments were performed. First, we added different amounts of KaFe (0.0025−0.25 g) into 10 mL of 3.69×10^{-3} M $HgCl_2$ and sonicated the solutions for 10 min. These solutions were then centrifuged and diluted 13 times with Milli-Q water to record UV−vis spectra. With increasing KaFe, the absorption of [$HgCl_2$] was increased and an increasing amount of Hg(II) was removed from the solution, as seen in Figure 8A. Again, for a fixed amount of KaFe (0.01 g), we repeated a few experiments with varying concentrations of $HgCl_2$, as illustrated in Figure 8B. We discovered that the extent of absorption remains almost unchanged with the variation of [$HgCl_2$]. Figure 8C shows almost parallel lines of absorbance for only $HgCl_2$ and $HgCl_2$+KaFe, at different concentrations of $HgCl_2$. $Hg(NO_3)_2$ and $HgBr_2$ were also tested in the context of absorption with KaFe. It was discovered that all Hg(II) salts were absorbed significantly in KaFe, as illustrated in Figure S13. However, these Hg(II) salts, except for $HgCl_2$, could not form HEIN.

2.8. Impact of Other Metal Halides on the Absorption in KaFe. We attempted to evaluate the impacts of different metal chlorides [copper(II) chloride, sodium(I) chloride, aluminum-(III) chloride, nickel(II) chloride, cobalt(II) chloride, chromium(II) chloride, potassium(I) chloride, calcium(II) chloride, magnesium(II) chloride, tin(II) chloride] in the context of absorption in KaFe. We observed from UV−vis spectral analysis that $SnCl_2$, $CuCl_2$, $CrCl_3$, and $AlCl_3$ were also absorbed significantly in KaFe, like $HgCl_2$. However, no metal chloride (except $HgCl_2$) could produce HEIN, as shown in Figure S14.

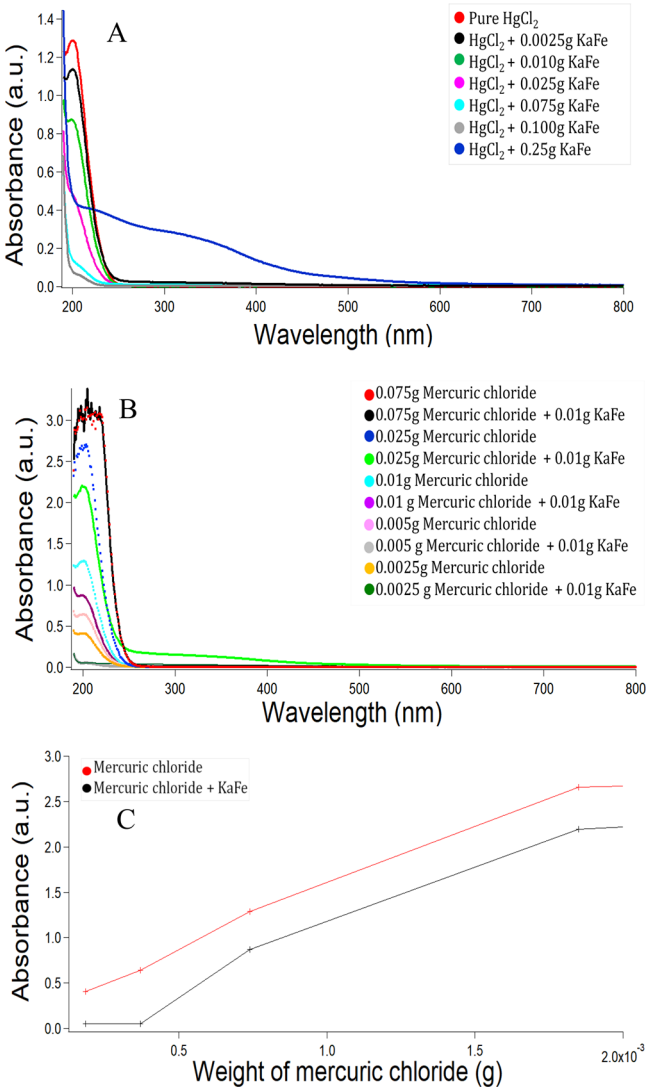

Figure 8. (A) UV−vis spectra of $HgCl_2$ in the presence of different amounts of KaFe (spectra have been recorded after 13 times dilution), [$HgCl_2$] = 2.84×10^{-4} M. (B) UV−vis spectra of different amounts of $HgCl_2$ in the presence and absence of fixed amount of KaFe (spectra have been recorded after 13 times dilution). (C) Comparative study of absorbance variation with different amounts of $HgCl_2$ (with and without KaFe) as mentioned in (B).

2.9. Effect of Chelation. Hg(II) forms a strong chelate with disodium ethylene diamine tetra acetic acid (Na_2-EDTA).[42,43] Having this idea in mind, we prepared a Hg(II)−EDTA complex by mixing Na_2−EDTA and $HgCl_2$ in a 1:1 molar ratio in Milli-Q water. Therefore, the water solution containing [Hg(II)-EDTA]Cl_2 and KaFe resulted in an average ice nucleating material (−14.9 to −8.7 °C; MFT, −12.3 °C) compared to HgKaFe. Experimental results indicated the necessity of having free Hg(II) in a solution to produce HEIN. From the UV−vis spectroscopic data, it was found that the absorption spectrum of [Hg(II)−EDTA]Cl_2 was almost unaltered after sonication with KaFe, implying that [Hg(II)−EDTA]Cl_2 would likely not be absorbed by KaFe (Figure 9).

2.10. Potential Reaction Mechanism. HgKaFe is a HEIN and is more efficient than any mineral dust or metal particle, which has been previously studied. The efficiency of HgKaFe, as an ice nucleating particle, is very close to the most efficient, but most rare ice nucleating particles in nature, biological particles. It

DOI: 10.1021/acsomega.7b01830
ACS Omega 2018, 3, 3384−3395

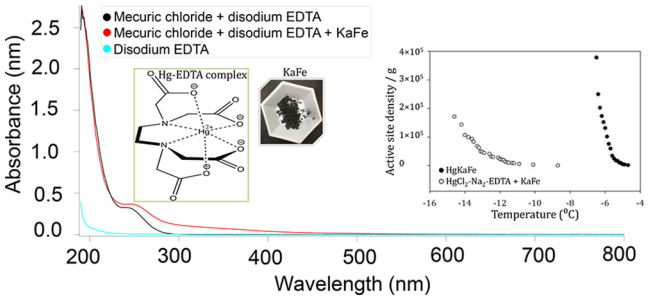

Figure 9. UV−vis spectra showing the absorption of Hg−EDTA complex on KaFe; [Hg(II)] = 1.42×10^{-4} M, KaFe = 0.01 g. The inset shows the comparison of the active-site density per gram and temperature to show the effect of Na_2−EDTA; [Hg(II)] = 3.69×10^{-3} M, KaFe = 0.0025 g, Milli-Q water = 10 mL.

was found that maghemite and Hg_2Cl_2 were the main constituents of HgKaFe, as mentioned below. However, it is still being explored if the mixture of the final products together or alone (in the presence of the other constituents, i.e., synergism) or any secondary product is the potential ice nucleating particle.

The two highly conversed "criteria" for efficient ice nucleating particles are the crystallographic match with respect to bulk ice and the strength of the water−surface interactions. As water−surface interaction is poorer for HgKaFe than for KaFe (the contact angle is less for KaFe), the first criterion, in this case, may be the dominant criterion. The arrangement of different heights of atoms in the contact layer is called buckling, which is a significant factor for efficient nucleation. It has been observed that if the first water overlayer is not icelike, then efficient ice nucleation is possible for pronounced buckling of the contact layer. When the atomic arrangement in the contact region is similar, small lattice mismatch (δ) is the pivotal factor for being an efficient nucleating particle. Despite serious challenges from recent experiments and simulations for validation and the generalization of the concept, small lattice mismatch is still a primary cause of efficient ice nucleation.[44−50] When the arrangements of atoms in the contact area are alike, δ between the corresponding surface unit cells can be explained in a more rationalized manner as

$$\delta = \frac{a_s - a_i}{a_i} \quad (1)$$

where a_i and a_s represent the lattice parameters of a certain face of ice and the surface unit cells of the substrate, respectively.

All of these factors individually or together generate HgKaFe to be HEIN. The extraordinarily narrow freezing range of −6.6 to −4.7 °C is an indication of one kind of dominant ice nucleating particle in HgKaFe. Further experiments and theoretical studies are to be conducted, to design an unequivocal mechanism behind the formation of the HEIN.

From the ice nucleation data, it is evident that HgKaFe is an efficient ice nucleating agent. The goal of the paper is to understand the physicochemical properties of HgKaFe in the context of ice nucleation. We know that iron/iron oxides in different forms (namely, magnetite,[51,52] maghemite,[52] hematite,[52,53] Fe dust,[52] etc.) are commonly available in the atmosphere. Silver iodide (AgI) is a well-known cloud seeding material.[54] We measured ice nucleation efficiency of iron oxides (Table 1, Figure S15, Supporting Information) and AgI (Table 1, Figure S15, Supporting Information) in comparison to HgKaFe. The efficiency of the HgKaFe nucleation rate, with the same size and mass of droplet, is much better (>7 °C warmer) than iron oxides and closer to AgI.

Table 1. MFT of Different Samples of 0.0025 g in 10 mL of Milli-Q Water[a]

sample	Fe dust	magnetite	hematite	maghemite	AgI	HgMtFe
MTF (°C)	−12.9	−19.3	−14.2	−13.6	−3.8	−5.8

[a]HgKaFe was diluted 5 times to obtain total mass of 0.0025 g in 10 mL of milli-Q water.

In this paper, we are unveiling the formation of highly efficient ice nucleating particles, where environmentally abundant iron oxide has a key role in the presence of toxic mercury chloride. Moreover, kaolin and iron oxide are very common ingredients in dust particles. Mercury in different forms is being emitted every day, creating a great threat to the environment.[55] The importance of the contact angle, surface sites, composition, and morphology on ice nucleation efficiency and untangling these effects from each other were the main theme of the work. These insights can be applied to atmospheric particles.

3. CONCLUSIONS AND FUTURE DIRECTIONS

Maghemite and Hg_2Cl_2 were key players in the preparation of highly efficient, completely inorganic ice nucleating particles. This new heterogeneous highly efficient ice nucleus was not associated with any biomolecule, which has been previously shown to be an efficient ice nucleating particle. No other studied metal ion was found to be able to make such an efficient ice nucleating particle, except mercury. Chloride also showed to play a pivotal role in ice nucleation. Kaolin−iron oxide composites absorbed $HgCl_2$ in an aqueous medium, and as a corollary, highly efficient ice nucleating particles were generated. Interactions of mineral dust particles (containing mostly iron oxide) with water vapor may alter heterogeneous reactivity toward toxic metals. Immersion freezing (ice nucleation by particles immersed in supercooled water) is a crucial route for creating ice in mixed-phase clouds. Immersion freezing experiments with particles in microliter-sized water droplets are often used for identifying very small numbers of nucleating particles. Additionally, atmospheric heterogeneous and multiphase reactions may influence the chemical compositions when mineral dust particles reach the troposphere. Therefore, interactions of mineral dust particles with water vapor are changed.

A complete and in-depth knowledge of the interactions between dust and dust containing toxic metals with water vapor will help us to understand the role mineral dust aerosols have in many facets of atmospheric chemistry. These important facets include the increasing threat of climate change and airborne nanoparticles near emission sources, including urban areas. These areas are major sites of important pollutants in climate change and environmental health. To conclude, a better understanding of nanoparticles in the atmosphere and ice nucleation may lead to an improvement in climate change and public health knowledge.

4. EXPERIMENTAL SECTION

In this section, we describe the synthesis methods, as well as various analytical techniques for chemical and physical analyses. Also, the materials and supplies required are discussed.

4.1. Synthesis. *4.1.1. Synthesis of KaFe.* $FeCl_2 \cdot 4H_2O$ (2.67 g) was fully dissolved in a 4:1 ethanol/water mixture (24 mL of ethanol and 6 mL of water). Consequently, 1.5 g of kaolin was

DOI: 10.1021/acsomega.7b01830
ACS Omega 2018, 3, 3384−3395

added to the solution, creating a muddy beige mixture. This suspension was then placed in an ultrasonic shaker for 2 h to disperse the kaolin particles. In the meantime, a 1 M $NaBH_4$ solution was prepared by dissolving 3.05 g of the powder in 100 mL of ice-cold Milli-Q water. When the ultrasonic shaking was completed, the freshly prepared sodium borohydride solution was added dropwise into the suspension with vigorous shaking, showing an instant color change from beige to black. When the entire $NaBH_4$ solution was transferred, the reaction mixture was shaken for 10 min and left to settle for 1 day. After 24 h, the supernate was decanted, while keeping the solid inside the container with a strong magnet, then the solid was washed eight times with 200 mL of Milli-Q water and twice with 200 mL of ethanol. The synthesized iron−kaolin composite was then placed in a vacuum oven at 50 °C to dry completely. Finally, when the drying process was complete, the solid was crushed and mixed thoroughly using a mortar and pestle to obtain KaFe.

4.1.2. Synthesis of BHFe. BHFe was synthesized using the same procedure as the KaFe synthesis; however, kaolin was not used.

4.1.3. Synthesis of HgKaFe. KaFe (0.0025 g) was sonicated with 10 mL of a 3.69×10^{-3} M aqueous $HgCl_2$ solution for 10 min to form HgKaFe.

4.2. Analytical Techniques for Physical and Chemical Characterization. *4.2.1. Drop-Freezing Assays.* Drop-freezing experiments are among the most common techniques to judge the ice nucleation efficiency of a heterogeneous ice nucleating particle in immersion mode.[19,24] A better method for gauging immersion freezing in large droplets over a wide temperature range has been shown by Tobo.[25] For each sample, droplets were placed on a cooling plate (in-house-made copper plate) and the plate (starting at ∼0 °C) was cooled at a rate of 1 °C/min. The temperature at which each droplet froze was recorded. The samples were loaded onto the plate as 10 μL droplets. Before adding the droplets, a thin layer of petroleum jelly was spread on the copper plate to minimize the reactions between the copper plate and the drops and to maintain hydrophobicity.

We followed the Tobo protocol[25] to plot ice nucleation data. It was assumed that the ice nucleation process by immersed particles in a supercooled drop was both a temperature-dependent and time-independent process. So, the cumulative number of ice nucleation active sites per unit volume of water (K) at a certain temperature (T) can be presented by the following equation (eq 2)

$$K(T) = -\frac{\ln(1 - f_{\text{frozen}}(T))}{V} \tag{2}$$

When the mass of particles per unit volume of water is known, the ice nucleation active-site density per unit mass (n_m) can also be expressed by eq 3

$$n_m(T) = -(K(T)d)/C_m \tag{3}$$

where C_m represents the mass concentration of the particles in the initial suspension and d represents the dilution ratio of the suspension relative to C_m. We have performed background corrections by subtracting the ice nucleation data of pure Milli-Q water.

4.2.2. UV−Vis Spectroscopy. All UV−vis absorption spectra were recorded on a Varian Cary 50 Bio UV spectrophotometer. The solutions were put into a 1 cm, well-stoppered quartz cuvette. The spectra were recorded against a reference solvent.

4.2.3. Contact Angle. Thin films of kaolin, KaFe, and HgKaFe were prepared on a glass slide using a spin coater. The contact angle was measured by placing 10 μL of Milli-Q water on the thin films using a Rame-Hart goniometer (model number 100-00115).

4.2.4. Scanning Electron Microscopy. Particle morphology was examined using an FEI Helios NanoLab 660 DualBeam (focused ion beam) extreme high-resolution scanning electron microscope. The microscope contains Leica Microsystems EM VCT100 Cryo Transfer System, MultiChem Gas Injection System, and EDAX Octane Ultra 100 mm^2 SDD and TEAM 3D EDS Analysis System. Samples of kaolin, KaFe, BHFe, and HgKaFe were vacuum-dried for 24 h before measurements were taken. The compounds were then coated with Pt and put on carbon tape before SEM studies were conducted.

4.2.5. Transmission Electron Microscopy. Samples of kaolin (0.0025 g in 10 mL of Milli-Q water), KaFe (0.0025 g in 10 mL of Milli-Q water), BHFe (0.0025 g in 10 mL of Milli-Q water), and HgKaFe (5 μL) were deposited on glow-discharged carbon film-coated copper electron microscopy grids. The droplets were kept on the grids for 1 min, followed by blotting off the excess liquid with the edge of a piece of filter paper. The samples were imaged using an FEI Tecnai 12 Biotwin TEM microscope (FEI Electron Optics) equipped with a tungsten filament at 120 kV, containing an AMT XR80C CCD Camera System.

4.2.6. X-ray Diffraction. X-ray diffraction (XRD) was performed with a Bruker D8 Discovery X-ray diffractometer (VANTEC Detector Cu-Source λ = 1.5418 Å). XRD patterns were recorded for $3° \leq 2\theta \leq 80°$ with increments of 0.005°. Samples of kaolin, KaFe, BHFe, and HgKaFe were vacuum-dried at room temperature before measurements were taken.

4.2.7. X-ray Photoelectron Spectroscopy. X-ray photoelectron spectroscopy (XPS) measurement was carried out with a Thermo Scientific K-Alpha X-ray photoelectron spectrometer. The samples were loaded onto carbon tape to be placed on a grid for the analysis. Samples of KaFe and HgKaFe were vacuum-dried at room temperature before measurement.

4.3. Materials and Supplies. All of the reagents were of analytical reagent grade, and Milli-Q water was used throughout the experiment. Kaolin, all metal salts, iron dust, all iron oxides, disodium ethylene diamine tetra acetic acid (Na_2-EDTA), and hydrogen peroxide were purchased from Sigma-Aldrich. Sodium borohydride was obtained from Alfa Aesar. All glassware was cleaned with freshly prepared aqua regia, subsequently rinsed with copious amounts of distilled water, and dried well before use. All of the reagents were used without further purification.

■ ASSOCIATED CONTENT

Supporting Information

The Supporting Information is available free of charge on the ACS Publications website at DOI: 10.1021/acsomega.7b01830.

Elemental analysis; XRD; XPS; ice nucleation data; IR; UV−vis spectra (PDF)

■ AUTHOR INFORMATION

Corresponding Author

*E-mail: parisa.ariya@mcgill.ca.

ORCID

Mainak Ganguly: 0000-0002-5315-7381

Notes

The authors declare no competing financial interest.

DOI: 10.1021/acsomega.7b01830
ACS Omega 2018, 3, 3384−3395

■ ACKNOWLEDGMENTS

This work was supported by the Natural Sciences and Engineering Research Council of Canada (NSERC)—NSERC CREATE Mine of Knowledge, Fonds de recherche du Québec—Nature et Technologies (FRQNT), and Environment Canada. The authors are thankful to Rangel-Alvarez for helping with thin-film preparation. They also thank Mr. Kurien and Ms. Morris for their valuable comments to improve the manuscript.

■ REFERENCES

(1) Grim, R. E. *Clay Mineraology*, 2nd ed.; McGraw Hill: New York, 1968; p 596.
(2) Rozenson, I.; Spiro, B.; Zak, I. Transformation of ironbearing kaolinite to iron-free kaolinite, goethite, and hematite. *Clays Clay Miner.* **1982**, *30*, 207−214.
(3) Goldbery, R. Sedimentology of the Lower Jurassic flint clay bearing Mishhor Formation, Makhtesh Ramon, Israel. *Sedimentology* **1979**, *26*, 229−251.
(4) Slatkine, A.; Heller, L. In *A Petrological Study of the Flint Clay from Makhtesh Ramon*, International Geological Congress 21st Session. Norden Part, 1961; Vol. *24*, pp 88−107.
(5) *Air Pollution from Electricity-Generating Large Combustion Plants*; European Environment Agency (EEA): Copenhagen, 2008, ISBN 978-92-9167-355-1.
(6) Adams, P. J.; Donahue, N. M.; Pandis, S. N. Atmospheric nanoparticles and climate change. *AIChE J.* **2013**, *59*, 4006−4019.
(7) Gwinn, M. R.; Vallyathan, V. Nanoparticles: health effects—pros and cons. *Environ. Health Perspect.* **2006**, *114*, 1818−1825.
(8) Saunders, R. W.; Mohler, O.; Schnaiter, M.; Benz, S.; Wagner, R.; Saathoff, H.; Connolly, P. J.; Burgess, R.; Gallagher, M.; Wills, R.; Murray, B. J.; Plane, J. M. C. Plane An aerosol chamber investigation of the heterogeneous ice nucleating potential of refractory nanoparticles. *Atmos. Chem. Phys. Discuss.* **2009**, *9*, 23271−23318.
(9) Harrison, R. G. Cloud formation and the possible significance of charge for atmospheric condensation and ice nuclei. *Space Sci. Rev.* **2000**, *94*, 381−396.
(10) Bartels-Rausch, T. Chemistry: Ten things we need to know about ice and snow. *Nature* **2013**, *494*, 27−29.
(11) Mazur, P. Cryobiology: The freezing of biological systems. *Science* **1970**, *168*, 939−949.
(12) McNeill, V. F.; Grannas, A. M.; Abbatt, J. P. D.; Ammann, M.; Ariya, P.; Bartels-Rausch, T.; Domine, F.; Donaldson, D. J.; Guzman, M. I.; Heger, D.; Kahan, T. F.; Klan, P.; Masclin, S.; Toubin, C.; Voisin, D. Organics in environmental ices: sources, chemistry, and impacts. *Atmos. Chem. Phys.* **2012**, *12*, 9653−9678.
(13) Vali, G.; DeMott, P. J.; Möhler, O.; Whale, T. F. Technical note: a proposal for ice nucleation terminology. *Atmos. Chem. Phys.* **2015**, *15*, 10263−10270.
(14) Mortazavi, R.; Hayes, C. T.; Ariya, P. A. Ice nucleation activity of bacteria isolated from snow compared with organic and inorganic substrates. *Environ. Chem.* **2008**, *5*, 373−381.
(15) Archuleta, C. M.; DeMott, P. J.; Kreidenweis, S. M. Ice nucleation by surrogates for atmospheric mineral dust and mineral dust/sulfate particles at cirrus temperatures. *Atmos. Chem. Phys. Discuss.* **2005**, *5*, 3391−3436.
(16) Zolles, T.; Burkart, J.; Hausler, T.; Pummer, B.; Hitzenberger, R.; Grothe, H. Identification of Ice Nucleation Active Sites on Feldspar Dust Particles. *J. Phys. Chem. A* **2015**, *119*, 2692−2700.
(17) Welti, A.; Kanji, Z. A.; Lüönd, F.; Stetzer, O.; Lohmann, U. Exploring the Mechanisms of Ice Nucleation on Kaolinite: From Deposition Nucleation to Condensation Freezing. *J. Atmos. Sci.* **2014**, *71*, 16−36.
(18) Salam, A.; Lesins, G.; Lohmann, U. Laboratory study of heterogeneous ice nucleation in deposition mode of montmorillonite mineral dust particles aged with ammonia, sulfur dioxide, and ozone at polluted atmospheric concentrations. *Air Qual., Atmos. Health* **2008**, *1*, 135−142.
(19) Rangel-Alvarado, R. B.; Nazarenko, Y.; Ariya, P. A. Snow-borne nanosized particles: Abundance, distribution, composition, and significance in ice nucleation processes. *J. Geophys. Res.: Atmos.* **2015**, *120*, 11760−11774.
(20) Ariya, P. A.; Amyot, M.; Dastoor, A.; Deeds, D.; Feinberg, A.; Kos, G.; Poulain, A.; Ryjkov, A.; Semeniuk, K.; Subir, M.; Toyota, K. Mercury physicochemical and biogeochemical transformation in the atmosphere and at atmospheric interfaces: a review and future directions. *Chem. Rev.* **2015**, *115*, 3760−3802.
(21) Ponder, S. M.; Darab, J. G.; Mallouk, T. E. Remediation of Cr(VI) and Pb(II) aqueous solutions using supported, nanoscale zero-valent iron. *Environ. Sci. Technol.* **2000**, *34*, 2564−2569.
(22) Kanel, S. R.; Manning, B.; Charlet, L.; Choi, H. Removal of arsenic(III) from groundwater by nanoscale zero-valent iron. *Environ. Sci. Technol.* **2005**, *39*, 1291−1298.
(23) Liu, T.; Xue, L.; Guo, X.; Huang, Y.; Zheng, C. DFT and experimental study on the mechanism of elemental mercury capture in the presence of HCl on α-Fe_2O_3(001). *Environ. Sci. Technol.* **2016**, *50*, 4863−4868.
(24) Vali, G. Quantitative Evaluation of Experimental Results and the Heterogeneous Freezing Nucleation of Supercooled Liquids. *J. Atmos. Sci.* **1971**, *28*, 402−409.
(25) Tobo, Y. An improved approach for measuring immersion freezing in large droplets over a wide temperature range. *Sci. Rep.* **2016**, *6*, No. 32930.
(26) Brooks, S. D.; Suter, K.; Olivarez, L. Effects of Chemical Aging on the Ice Nucleation Activity of Soot and Polycyclic Aromatic Hydrocarbon Aerosols. *J. Phys. Chem. A* **2014**, *118*, 10036−10047.
(27) Salazar-Alvarez, G.; Sort, J.; Uheida, A.; Muhammed, M.; Surinach, S.; Baro, M. D.; Nogues, J. Reversible post-synthesis tuning of the superparamagnetic blocking temperature of γ-Fe_2O_3 nanoparticles by adsorption and desorption of Co(II) ions. *J. Mater. Chem.* **2007**, *17*, 322−328.
(28) Han, C.; Ma, J.; Wu, H.; Wei, Y.; Hu, K. A low-cost and high-yield production of magnetite nanorods with high saturation magnetization. *J. Chil. Chem. Soc.* **2015**, *60*, 2799−2802.
(29) Ivanova, A. S.; Slavinskaya, E. M.; Stonkus, O. A.; Gulyaev, R. V.; Glazneva, T. S.; Noskova, A. S.; Boronin, A. I. Highly active and durable Pd/Fe_2O_3 catalysts for wet CO oxidation under ambient conditions. *Catal. Sci. Technol.* **2016**, *6*, 3918−3928.
(30) David, B.; Pizúrová, N.; Synek, P.; Kudrle, V.; Jašekb, O.; Schneeweissa, O. epsilon-Fe2O3 nanoparticles synthesized in atmospheric-pressure microwave torch. *Mater. Lett.* **2014**, *116*, 370−373.
(31) Moussy, J.-B. From epitaxial growth of ferrite thin films to spinpolarized tunnelling. *J. Phys. D: Appl. Phys.* **2013**, *46*, No. 143001.
(32) Liu, J.; Du, X. Fast removal of aqueous Hg(II) with quaternary ammonium-functionalized magnetic mesoporous silica and silica regeneration. *J. Mater. Chem.* **2011**, *21*, 6981−6987.
(33) Sharma, R. K.; Rastogi, A. C.; Desu, S. B. Manganese oxide embedded polypyrrole nanocomposites for electrochemical supercapacitor. *Electrochim. Acta* **2008**, *53*, 7690−7695.
(34) Chopra, T. P.; Longo, R. C.; Cho, K.; Halls, M. D.; Thissen, P.; Chabal, Y. J. Ethylenediamine grafting on oxide-free H-, 1/3 ML F-, and Cl-terminated Si(111) surfaces. *Chem. Mater.* **2015**, *27*, 6268−6281.
(35) Lupi, L.; Molinero, V. Does hydrophilicity of carbon particles improve their ice nucleation ability? *J. Phys. Chem. A* **2014**, *118*, 7330−7337.
(36) Whale, T. F.; Rosillo-Lopez, M.; Murray, B. J.; Salzmann, C. G. Ice nucleation properties of oxidized carbon nanomaterials. *J. Phys. Chem. Lett.* **2015**, *6*, 3012−3016.
(37) Zhang, W. X. J. Nanoscale iron particles for environmental remediation: an overview. *J. Nanopart. Res.* **2003**, *5*, 323−332.
(38) Tratnyek, P. G.; Johnson, R. L. Nanotechnologies for environmental cleanup. *Nano Today* **2006**, *1*, 44−48.
(39) Üzüm, Ç.; Shahwan, T.; Eroğlu, A. E.; Hallam, K. R.; Scott, T. B.; Lieberwirth, I. Synthesis and characterization of kaolinite-supported zero-valent iron nanoparticles and their application for the removal of aqueous Cu2+ and Co2+ ions. *Appl. Clay Sci.* **2009**, *43*, 172−181.

DOI: 10.1021/acsomega.7b01830
ACS Omega 2018, 3, 3384−3395

(40) Zhang, H.; Jin, Z. H.; Han, L.; Qin, C. H. Synthesis of nanoscale zero-valent iron supported on exfoliated graphite for removal of nitrate. *Trans. Nonferrous Met. Soc. China* **2006**, *16*, S345−S349.
(41) Zhou, X.; Zeng, K.; Wanga, Q.; Yang, X.; Wang, K. In vitro studies on dissolved substance of cinnabar: Chemical species and biological properties. *J. Ethnopharmacol.* **2010**, *131*, 196−202.
(42) Ganguly, M.; Mondal, C.; Pal, J.; Pal, A.; Negishi, Y.; Pal, T. Fluorescent Au(I)@Ag_2/Ag_3 giant cluster for selective sensing of mercury(II) ion. *Dalton Trans.* **2014**, *43*, 11557−11565.
(43) Ganguly, M.; Mondal, C.; Jana, J.; Pal, A.; Pal, T. Selective dopamine chemosensing using silver-enhanced fluorescence. *Langmuir* **2014**, *30*, 4120−4128.
(44) Fitzner, M.; Sosso, G. C.; Cox, S. J.; Michaelides, A. The many faces of heterogeneous ice nucleation: interplay between surface morphology and hydrophobicity. *J. Am. Chem. Soc.* **2015**, *137*, 13658−13669.
(45) Murray, B. J.; O'Sullivan, D.; Atkinson, J. D.; Webb, M. E. Ice nucleation by particles immersed in supercooled cloud droplets. *Chem. Soc. Rev.* **2012**, *41*, 6519−6554.
(46) Zettlemoyer, A. C.; Tcheurekdjian, N.; Chessick, J. Surface properties of silver iodide. *Nature* **1961**, *192*, 653.
(47) Fraux, G.; Doye, J. P. K. Heterogeneous ice nucleation on silver-iodide-like surfaces. *J. Chem. Phys.* **2014**, *141*, No. 216101.
(48) Cabriolu, R.; Li, T. Ice nucleation on carbon surface supports the classical theory for heterogeneous nucleation. *Phys. Rev. E* **2015**, *91*, No. 052402.
(49) Cox, S. J.; Kathmann, S. M.; Purton, J. A.; Gillan, M. J.; Michaelides, A. Non-hexagonal ice at hexagonal surfaces: the role of lattice mismatch. *Phys. Chem. Chem. Phys.* **2012**, *14*, 7944−7949.
(50) Cox, S. J.; Raza, Z.; Kathmann, S. M.; Slater, B.; Michaelides, A. The microscopic features of heterogeneous ice nucleation may affect the macroscopic morphology of atmospheric ice crystals. *Faraday Discuss.* **2013**, *167*, 389−403.
(51) Maher, B. A.; Ahmed, I. A. M.; Karloukovski, V.; MacLaren, D. A.; Foulds, P. G.; Allsop, D.; Mann, D. M. A.; Torres-Jardon, R.; Calderon-Garciduenas, L. Magnetite pollution nanoparticles in the human brain. *Proc. Natl. Acad. Sci. U. S. A.* **2016**, *113*, 10797−10801.
(52) Moreno, T.; Martins, V.; Querol, X.; Jones, T.; BeruBe, K.; Minguillon, M. C.; Amato, F.; Capdevila, M.; de Miguel, E; Centelles, S.; Gibbons, W. A new look at inhalable metalliferous airborne particles on rail subway platforms. *Sci. Total Environ.* **2015**, *505*, 367−375.
(53) Flament, P.; Mattielli, N.; Aimoz, L.; Choel, M.; Deboudt, K.; de Jong, J.; Rimetz-Planchon, J.; Weis, D. Iron isotopic fractionation in industrial emissions and urban aerosols. *Chemosphere* **2008**, *73*, 1793−1798.
(54) Marcolli, C.; Nagare, B.; Welti, A.; Lohman, U. Iron isotopic fractionation in industrial emissions and urban aerosols. *Atmos. Chem. Phys.* **2016**, *16*, 8915−8937.
(55) Streets, D. G.; Devane, M. K.; Lu, Z.; Bond, T. C.; Sunderland, E. M.; Jacob, D. J. All-time releases of mercury to the atmosphere from human activities. *Environ. Sci. Technol.* **2011**, *45*, 10485−10491.

DOI: 10.1021/acsomega.7b01830
ACS Omega 2018, 3, 3384−3395